

A Novel Magnetic Hardening Mechanism for Nd-Fe-B Permanent Magnets Based on Solid-State Phase Transformation

Lukas Schäfer,* Konstantin Skokov, Fernando Maccari, Iliya Radulov, David Koch, Andrey Mazilkin, Esmaeil Adabifroozjaei, Leopoldo Molina-Luna, and Oliver Gutfleisch

Permanent magnets based on neodymium-iron-boron (Nd-Fe-B) alloys provide the highest performance and energy density, finding usage in many high-tech applications. Their magnetic performance relies on the intrinsic properties of the hard-magnetic $\text{Nd}_2\text{Fe}_{14}\text{B}$ phase combined with control over the microstructure during production. In this study, a novel magnetic hardening mechanism is described in such materials based on a solid-state phase transformation. Using modified Nd-Fe-B alloys of the type $\text{Nd}_{16}\text{Fe}_{\text{bal-x-y-z}}\text{Co}_x\text{Mo}_y\text{Cu}_z\text{B}_7$ for the first time it is revealed how the microstructural transformation from the metastable $\text{Nd}_2\text{Fe}_{17}\text{B}_x$ phase to the hard-magnetic $\text{Nd}_2\text{Fe}_{14}\text{B}$ phase can be thermally controlled, leading to an astonishing increase in coercivity from $\approx 200 \text{ kAm}^{-1}$ to almost 700 kAm^{-1} . Furthermore, after thermally treating a quenched sample of $\text{Nd}_{16}\text{Fe}_{56}\text{Co}_{20}\text{Mo}_2\text{Cu}_2\text{B}_7$, the presence of Mo leads to the formation of fine FeMo_2B_2 precipitates, in the range from micrometers down to a few nanometers. These precipitates are responsible for the refinement of the $\text{Nd}_2\text{Fe}_{14}\text{B}$ grains and so for the high coercivity. This mechanism can be incorporated into existing manufacturing processes and can prove to be applicable to novel fabrication routes for Nd-Fe-B magnets, such as additive manufacturing.

electricity, from wind, waves, and hydro, and to consume it, in transportation, buildings, and clean-tech.^[1–3] Most Nd-Fe-B magnets are sintered, with the grain size of the hard-magnetic $\text{Nd}_2\text{Fe}_{14}\text{B}$ phase being in the range of 2–10 μm .^[1,4–6] There are some alternative process routes, for example, the hot deformation can produce textured Nd-Fe-B magnets with grain sizes in the sub-micrometer range.^[7,8] But irrespective of the way the magnets are made, the $\text{Nd}_2\text{Fe}_{14}\text{B}$ grains are separated by a few-nanometer-thick Nd-rich grain-boundary layer, which reduces the presence of defects on the surfaces of the hard magnetic grains, decouples these grains, and helps prevent the nucleation of reverse magnetic domains in a demagnetizing field, which then leads to a high coercivity.^[9,10]

The goal of all permanent-magnet fabrication processes is to create an ideal microstructure that maximizes both the coercivity and the remanence, resulting

in the highest energy density. This ideal microstructure can be approximated with multi-step powder-metallurgy, but not by simply heat-treating ingots in the as-cast state, nor with any of the additive-manufacturing techniques like powder-bed fusion that melt the powders with a laser. This is because melting

1. Introduction

With their large energy density, neodymium-iron-boron (Nd-Fe-B) permanent magnets are central to our renewable-energy future. They are used in countless applications to generate


L. Schäfer, K. Skokov, F. Maccari, I. Radulov, O. Gutfleisch
Functional Materials
Institute of Material Science
Technical University of Darmstadt
64287, Darmstadt, Germany
E-mail: lukas.schaefer@tu-darmstadt.de

D. Koch
Structure Research
Institute of Material Science
Technical University of Darmstadt
64287, Darmstadt, Germany

A. Mazilkin
Institute of Nanotechnology
Karlsruhe Institute of Technology
76344, Eggenstein-Leopoldshafen, Germany

A. Mazilkin
Karlsruhe Nano Micro Facility (KNMFi)
Karlsruhe Institute of Technology
76344, Eggenstein-Leopoldshafen, Germany

E. Adabifroozjaei, L. Molina-Luna
Advanced Electron Microscopy
Institute of Material Science
Technical University of Darmstadt
64287, Darmstadt, Germany

 The ORCID identification number(s) for the author(s) of this article can be found under <https://doi.org/10.1002/adfm.202208821>.

© 2022 The Authors. Advanced Functional Materials published by Wiley-VCH GmbH. This is an open access article under the terms of the Creative Commons Attribution-NonCommercial-NoDerivs License, which permits use and distribution in any medium, provided the original work is properly cited, the use is non-commercial and no modifications or adaptations are made.

DOI: 10.1002/adfm.202208821

the Nd₂Fe₁₄B phase results in a complex solidification path, which is made more problematic by the line-compound nature of the Nd₂Fe₁₄B phase.^[11–13] Attempts to additively manufacture Nd-Fe-B magnets have proved to be frustrating, with the resulting microstructures containing many unwanted features that negatively affect the magnetic properties and especially the coercivity: the non-optimal grain size, poor redistribution of paramagnetic grain-boundary phases and the presence of soft-magnetic phases, e.g., α -Fe. Achieving a high coercivity with laser-melted magnets requires a new approach. If the coercivity cannot be based solely on creating isolated, micrometer grains, magnetic hardening based on precipitation with a phase-decomposition reaction would appear to be a possibility worth exploring. Here, we can take encouragement from the fact that the creation of a complex, coherent nanostructure has been possible with both Sm₂Co₁₇-type and Alnico magnets.^[14,15]

In this study we show the magnetic hardening of Nd-Fe-B-based bulk alloys via the formation of a metastable Nd₂Fe₁₇B_x phase in rapidly solidified cast alloys,^[16–33] which can subsequently be transformed during a heat treatment into magnetically decoupled Nd₂Fe₁₄B grains together with nanometer-sized, inter- and intragranular precipitates. With a degree of compositional modification of the Nd-Fe-B alloys we achieved a coercivity of ≈ 670 kAm⁻¹ without the need for a multi-step powder-metallurgy process or an expensive hot-pressing and die-upsetting procedure.

2. Rapid Solidification of Nd–Fe–Co–Mo–Cu–B Alloys and the Formation of a Metastable Nd₂Fe₁₇B_x Phase

Cast Nd–Fe–B alloys tend to have a dendritic microstructure in which the Nd₂Fe₁₄B grains are magnetically coupled due to a non-ideal redistribution of the paramagnetic, Nd-rich grain-boundary phase. As a result, the coercivity of cast or laser-melted materials is very low. Furthermore, it is not possible to achieve the desired microstructure with a subsequent heat treatment. We decided on a different approach and took advantage of the fact that undercooling the melt can lead to the formation of micrometer-sized grains of the metastable Nd₂Fe₁₇B_x phase. Upon subsequent annealing, the Nd₂Fe₁₇B_x \rightarrow Nd₂Fe₁₄B phase transformation can create the desired microstructure in which the newly formed Nd₂Fe₁₄B grains are magnetically decoupled. During the undercooling, the metastable Nd₂Fe₁₇B_x phase competes with the formation of α -Fe and Nd₂Fe₁₄B.

To obtain a large fraction of the metastable Nd₂Fe₁₇B_x phase, we quenched small pieces of Nd-Fe-B-based alloys (0.5–1 g) sealed in evacuated quartz ampules. These samples were remelted in a resistance furnace at 1300 °C for 10 min and subsequently quenched into water at room temperature. This simple experimental method allows us to imitate the “containerless” solidification techniques used by others to obtain the metastable Nd₂Fe₁₇B_x phase.^[16–33]

As part of our alloy-design strategy we investigated how modifying the composition of Nd-Fe-B alloys by adding Co, Mo and Cu can enhance the fraction of the metastable Nd₂Fe₁₇B_x phase in the as-quenched state, with the formation of the Nd₂Fe₁₄B phase upon subsequent annealing. The addition of Co

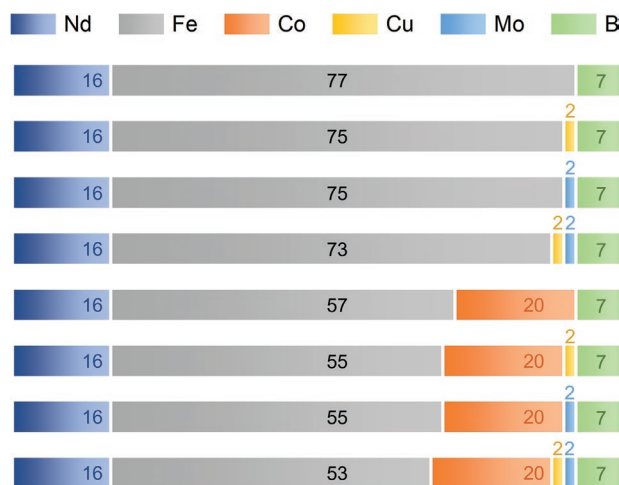


Figure 1. Overview of the sample compositions (in at. %). Nd (16 at. %) and B (7 at. %) contents were kept constant. The additions of Mo and Cu (2 at. % each) were at the expense of Fe. The Co concentration was kept constant at 20 at. %.

to the Nd–Fe–B system is known to stabilize the Nd₂(Fe,Co)₁₇ phase.^[34–38] In order to be consistent with the existing literature, we have adopted the categorization of Fidler & Schrefl^[10] where Cu (referred to as “type-I” element) is known to form low-melting-point rare-earth eutectics, which improve the wettability of the grains and lead to grain refinement (and so to a higher coercivity). On the other hand, Mo (referred to as a “type-II” element) has low solubility in the Nd₂Fe₁₄B phase and so has the potential to form precipitates. In all our samples, the Nd:B ratio was kept constant, which means that only the proportions of the transition metals were changed. An overview of these compositions with the systematic substitution of Fe with Mo and Cu is presented in **Figure 1**. This series is compared with a quaternary Nd-Fe-Co-B composition that has the same modifications involving Mo and Cu in **Figure 1**.

An annealing process was applied to each sample, similar to that is used in the production of sintered permanent magnets: high-temperature annealing at 1075 °C for 30 min, followed by cooling at 300 K h⁻¹ to 500 °C, dwell for 1 h and then furnace cooling to room temperature. The Co-free compositions are shown on the left-hand side of **Figure 2** (images a, c, e, g). The Nd₁₆Fe₇₇B₇ ternary sample (**Figure 2a**) is followed by the Cu-added Nd₁₆Fe₇₅Cu₂B₇ (**Figure 2c**), the Mo-added Nd₁₆Fe₇₅Mo₂B₇ (**Figure 2e**) and the sample with both Cu and Mo added Nd₁₆Fe₇₃Cu₂Mo₂B₇ (**Figure 2g**). The microstructures of the Co-doped samples with Nd₁₆Fe₅₇Co₂₀B₇, Nd₁₆Fe₅₅Co₂₀Cu₂B₇, Nd₁₆Fe₅₅Co₂₀Mo₂B₇, and Nd₁₆Fe₅₃Co₂₀Cu₂Mo₂B₇ (**Figure 2b,d,f,h**) are shown on the right side of **Figure 2**.

For the ternary Nd–Fe–B alloy, globular α -Fe appears in the dark BSE contrast, the matrix Nd₂Fe₁₄B phase is grey, while the bright contrast corresponds to the Nd-rich grain-boundary phase. The additions of Cu (**Figure 2c**) and both Cu and Mo (**Figure 2g**) lead to a refined microstructure, but dendritic α -Fe remains as the primary solidification product. The only exception was the Nd₁₆Fe₇₅Mo₂B₇ sample (**Figure 2e**), where the metastable Nd₂Fe₁₇B_x phase was the primary solidification product, rather than the α -Fe. The right-hand images

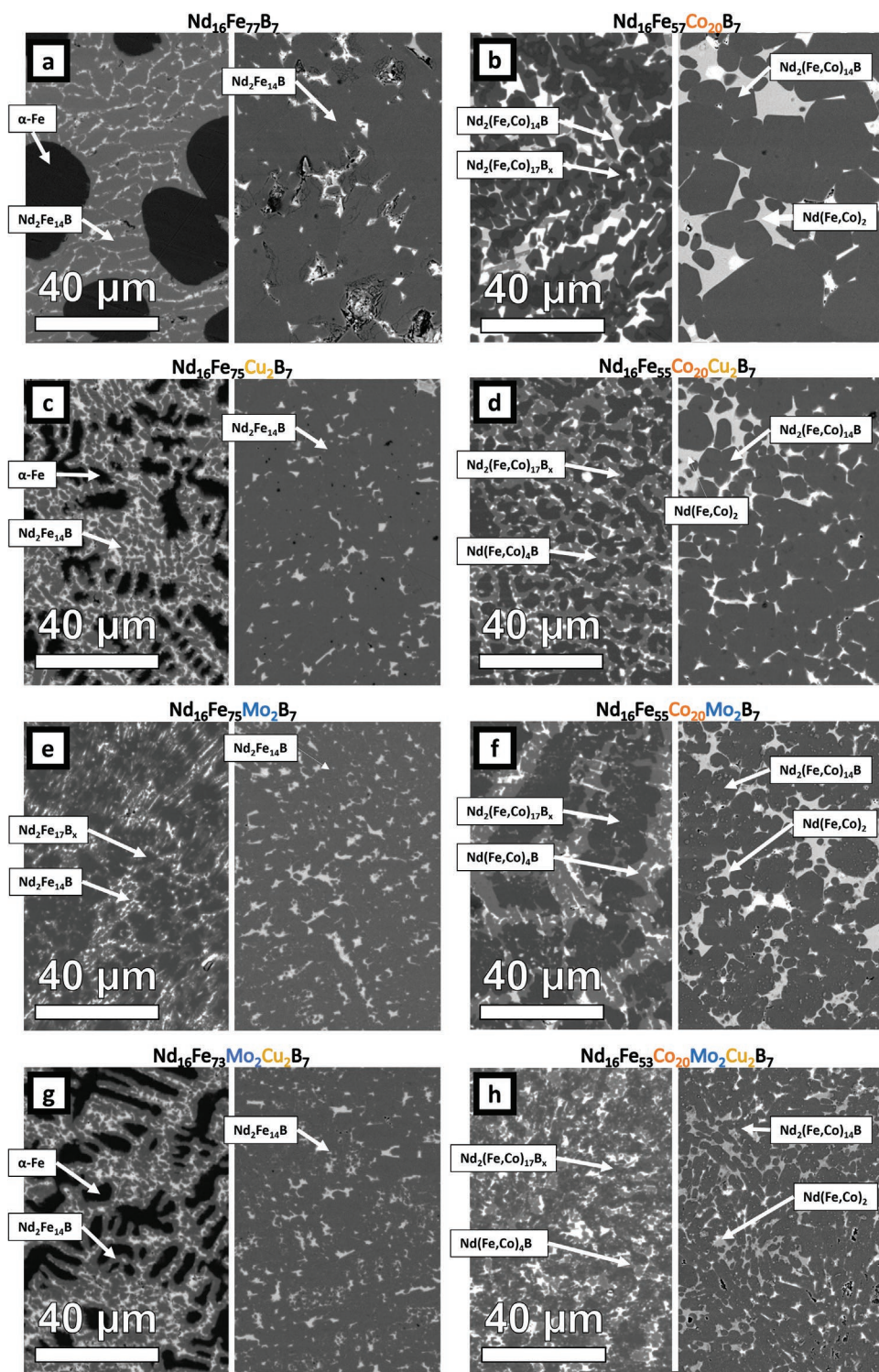


Figure 2. Microstructures of $\text{Nd}_{16}\text{Fe}_{\text{bal-x-y-z}}\text{Co}_x\text{Mo}_y\text{Cu}_z\text{B}_7$ samples (BSE-SEM contrast) after quenching from liquid state (left frame) and after annealing (right frame). The left-hand column (a,c,e,g) represents the alloys without Co substitution, whereas the right-hand column shows the Co-containing samples (b,d,f,h).

(Figure 2a,c,e,g) show the microstructure of these same samples after annealing. All the samples consist of the hard-magnetic $\text{Nd}_2\text{Fe}_{14}\text{B}$ grains and a Nd-rich phase, with both the metastable $\text{Nd}_2\text{Fe}_{17}\text{B}_x$ and $\alpha\text{-Fe}$ phases being fully transformed

by the heat treatment. The Mo addition leads to grain refinement of the $\text{Nd}_2\text{Fe}_{14}\text{B}$ phase after the heat treatment.

The addition of Co changes the solidification behavior of the samples. The quenched sample (Figure 2b) shows grains

with a core-shell structure. In the center of the grains the dark $\text{Nd}_2(\text{Fe},\text{Co})_{17}\text{B}_x$ phase was observed, whereas the rim of the grains was the $\text{Nd}_2(\text{Fe},\text{Co})_{14}\text{B}$ phase. Introducing both Co and Cu (Figure 2d) leads to a grain-refining effect, whereas the microstructure coarsens with the addition of Co and Mo (Figure 2f). The addition of Co, Cu, and Mo (Figure 2h) leads to a very fine microstructure consisting of $\text{Nd}_2(\text{Fe},\text{Co})_{17}\text{B}_x$ grains surrounded by the $\text{Nd}(\text{Fe},\text{Co})_4\text{B}$ and Nd-rich phases after quenching.

After annealing the Co-containing alloys, a bimodal size distribution with grains larger than $40\ \mu\text{m}$ and smaller than $5\ \mu\text{m}$ was found for the $\text{Nd}_{16}\text{Fe}_{57}\text{Co}_{20}\text{B}_7$ sample (Figure 2b). The grain-boundary phases are Nd-rich (very bright contrast) and $\approx\text{Nd}_{33}(\text{Fe},\text{Co})_{\text{bal}}$ (dark-grey contrast). Although the binary NdFe_2 Laves phase does not exist under equilibrium conditions, the EDX result indicates the formation $\text{Nd}(\text{Fe},\text{Co})_2$ phase in the Co-containing alloys, which was confirmed by X-ray diffraction (XRD). The corresponding diffractograms of the samples in the quenched state are shown in Figure S2 and after annealing treatment in Figure S3 (Supporting Information). The addition of Cu, Mo, and both Mo and Cu leads to a grain-refining effect, and in the $\text{Nd}_{16}\text{Fe}_{53}\text{Co}_{20}\text{Cu}_2\text{Mo}_2\text{B}_7$ sample (Figure 2h) the $\text{Nd}_2(\text{Fe},\text{Co})_{14}\text{B}$ grain size is below $10\ \mu\text{m}$. In addition, these grains are well separated by the (Nd,Cu)-rich and $\text{Nd}(\text{Fe},\text{Co})_2$ grain-boundary phases, so resembling the microstructure of a sintered Nd–Fe–B magnet.

X-ray diffraction analyses (XRD) were used for all the as-quenched and the annealed samples to identify the phases. The corresponding phase fractions were obtained by a combination of EDX, XRD, and image processing based on a Trainable Weka Segmentation,^[39] and are shown in Figure 3. After annealing, the $\text{Nd}_2\text{Fe}_{14}\text{B}$ phase occupied the largest fraction for all the samples. The Nd-rich phase was present in all the annealed alloys, although in the Co-containing alloys the fraction was very small due to the formation of the $\text{Nd}(\text{Fe},\text{Co})_2$ phase. In the $\text{Nd}_{16}\text{Fe}_{53}\text{Co}_{20}\text{Cu}_2\text{B}_7$ alloy the hexagonal $\text{Nd}(\text{Fe},\text{Co})_4\text{B}$ phase was detected, whereas in the annealed $\text{Nd}_{16}\text{Fe}_{55}\text{Co}_{20}\text{Mo}_2\text{B}_7$ and $\text{Nd}_{16}\text{Fe}_{53}\text{Co}_{20}\text{Cu}_2\text{Mo}_2\text{B}_7$ samples, there were traces of FeMo_2B_2 phase.

To understand the microstructural transformation during the heat treatment, thermomagnetic measurements were performed with the same quenched samples that were used for the microstructural analyses. At this point, it must be clarified that the heat treatment that the samples undergo during the measurement sequence does not result in any magnetic hardening. The corresponding measured hysteresis curves are shown in Figure S1 (Supporting Information) and show soft magnetic properties before and after heating the samples.

The heating (Figure 4, red lines) and cooling (Figure 4, blue lines) curves between 350 K and 1200 K were recorded in a magnetic field of 0.05 T. The magnetization is given in arbitrary units. The quenched ternary $\text{Nd}_{16}\text{Fe}_{77}\text{B}_7$ alloy (Figure 4a) can be taken as a reference sample. It shows only two Curie temperatures (T_C), corresponding to the $\text{Nd}_2\text{Fe}_{14}\text{B}$ ($T_C \sim 585\ \text{K}$) and $\alpha\text{-Fe}$ phases ($T_C \sim 1030\ \text{K}$). Similar behavior was observed for the $\text{Nd}_{16}\text{Fe}_{75}\text{Cu}_2\text{B}_7$ alloy in Figure 4c. Introducing Mo to the alloy leads to the formation of the metastable $\text{Nd}_2\text{Fe}_{17}\text{B}_x$ phase ($T_C \sim 375\ \text{K}$) in the $\text{Nd}_{16}\text{Fe}_{75}\text{Mo}_2\text{B}_7$ (Figure 4e) and $\text{Nd}_{16}\text{Fe}_{73}\text{Mo}_2\text{Cu}_2\text{B}_7$ (Figure 4g) alloys. It is important to mention that the formation of small amounts of metastable $\text{Nd}_2\text{Fe}_{17}\text{B}_x$ phase in the $\text{Nd}_{16}\text{Fe}_{73}\text{Mo}_2\text{Cu}_2\text{B}_7$ could only be detected with a sensitive thermomagnetic measurement, in addition to the XRD and SEM-BSE analysis (Figures 2 and 3).

The thermomagnetic measurements of the Nd–Fe–Co–B series (Figure 4, right-hand column) highlight the influence of Co on the Nd–Fe–B system. In the heating curve for $\text{Nd}_{16}\text{Fe}_{57}\text{Co}_{20}\text{B}_7$ (Figure 4b), two T_C are observed. The first T_C at approximately 710 K can be related to the $\text{Nd}_2(\text{Fe},\text{Co})_{17}\text{B}_x$ phase, followed by the T_C of the $\text{Nd}_2(\text{Fe},\text{Co})_{14}\text{B}$ phase ($\approx 760\ \text{K}$). With a further increase in the temperature, the magnetization increases again, due to the formation of the $\alpha\text{-}(\text{Fe},\text{Co})$ phase. In the Cu- and Mo-substituted samples (Figure 4d,f,h) the transition temperatures during the heating correspond to the $\text{Nd}_2(\text{Fe},\text{Co})_{17}\text{B}_x$ phase, whereas during cooling the T_C is that of the $\text{Nd}_2(\text{Fe},\text{Co})_{14}\text{B}$ phase, indicating the $\text{Nd}_2\text{Fe}_{17}\text{B}_x \rightarrow \text{Nd}_2\text{Fe}_{14}\text{B}$ solid-state reaction.

3. Magnetic Hardening of the $\text{Nd}_{16}\text{Fe}_{\text{bal-x-y-z}}\text{Co}_x\text{Mo}_y\text{Cu}_z\text{B}_7$ Samples

The hysteresis loops of the annealed samples are shown in Figure 5. The high initial magnetic susceptibility (the slope of the initial magnetization curve) from the thermally demagnetized

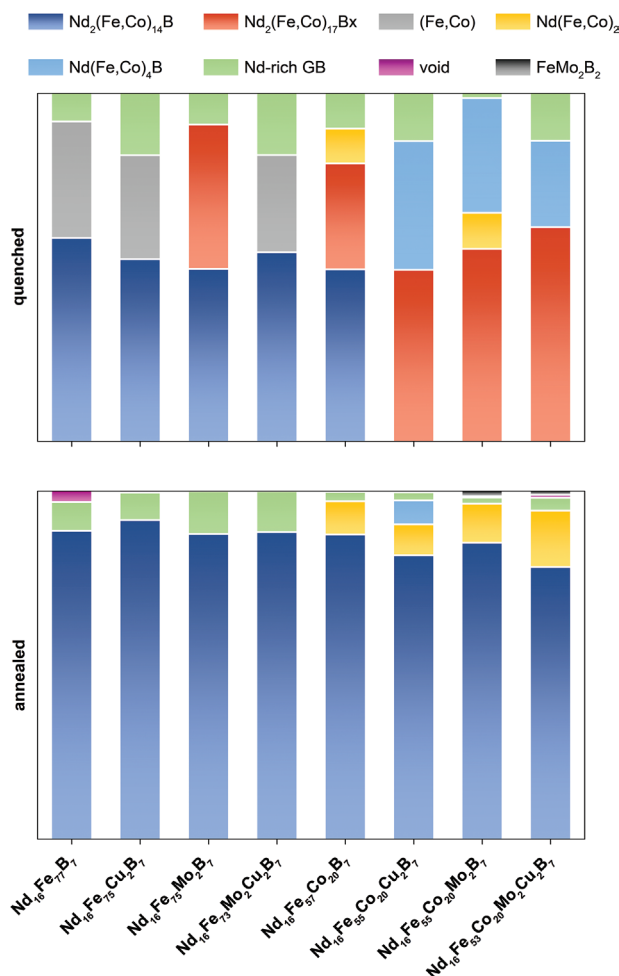


Figure 3. Phase fractions of the quenched samples (top) and annealed samples (bottom). The metastable $\text{Nd}_2\text{Fe}_{17}\text{B}_x$ phase is present in all the as-cast alloys that contain Co, and in the $\text{Nd}_{16}\text{Fe}_{75}\text{Mo}_2\text{B}_7$ alloy. After the heat treatment, the metastable $\text{Nd}_2\text{Fe}_{17}\text{B}_x$ is fully transformed into the $\text{Nd}_2\text{Fe}_{14}\text{B}$ and secondary intermetallic phases.

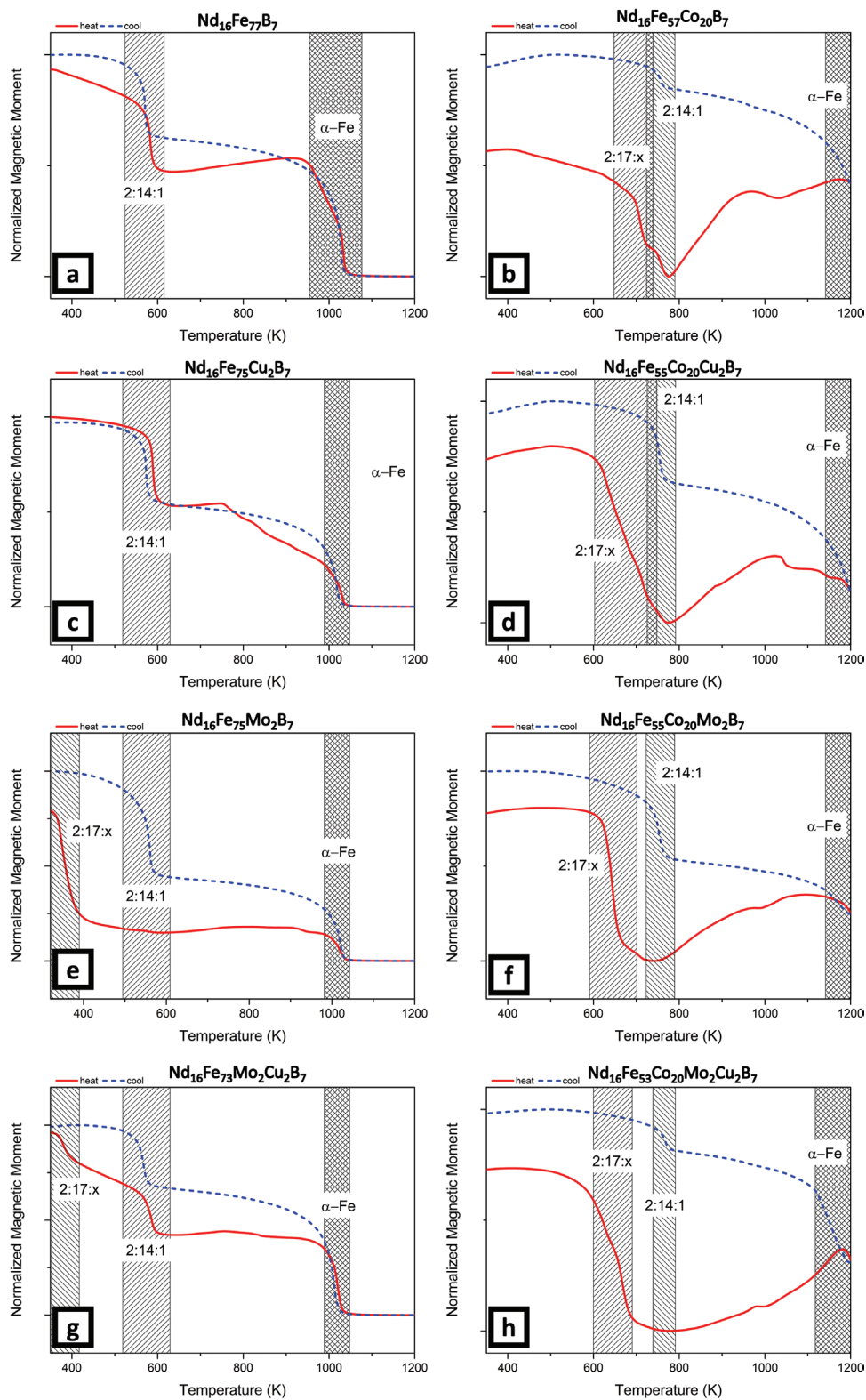


Figure 4. Thermomagnetic measurements of the quenched samples. The red lines are heating curves, whereas the blue lines are the cooling curves (the maximum temperature is 1200 K). The corresponding regions of the magnetic transitions are marked with shaded areas.

ized state indicates that all samples exhibit a nucleation-type coercivity mechanism. The coercivity values of the four samples without any Co addition (Figure 5a) do not exceed 250 kAm^{-1} .

Small variations in the absolute values can be attributed to slightly different grain sizes, and so are not significant. Figure 5b shows the hysteresis loops of the four Co-containing

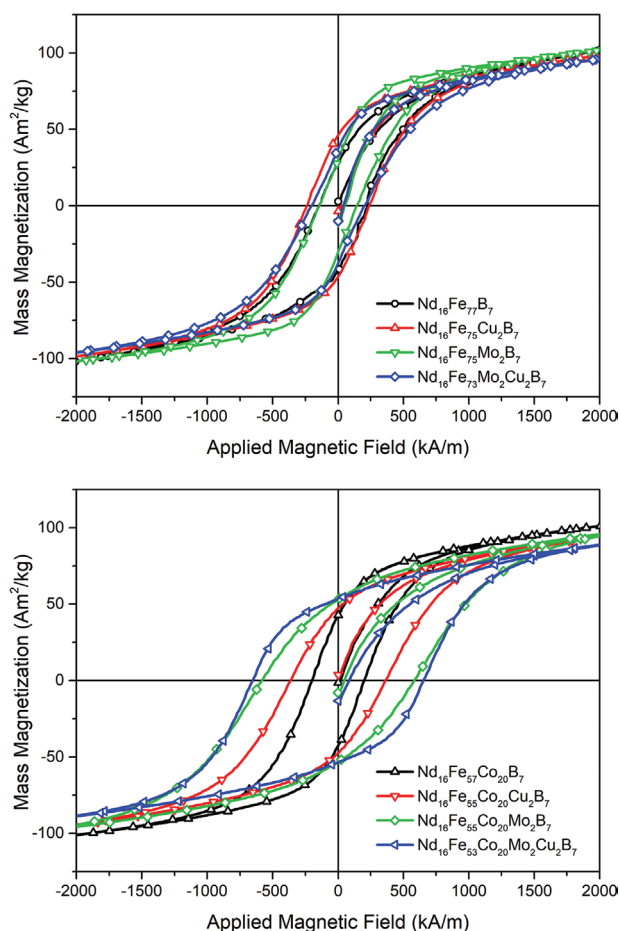


Figure 5. Hysteresis loops of the annealed samples without Co (top) and with Co (bottom). The alloys without Co show a maximum coercivity of approx. 250 kAm^{-1} , and additions of Cu and Mo do not lead to a significant change in the magnetic properties. In contrast, the addition of cobalt improves the coercivity, and simultaneous addition of Co, Mo, and Cu leads to the highest measured coercivity of around 670 kAm^{-1} .

samples. The addition of Co alone does not improve the magnetic properties: the coercivity of the $\text{Nd}_{16}\text{Fe}_{57}\text{Co}_{20}\text{B}_7$ sample (Figure 5b, black) is $\approx 200 \text{ kAm}^{-1}$. Only the combination of Co with Mo and/or Cu, plus the annealing treatment, leads to an astonishing improvement in the coercivity. For the $\text{Nd}_{16}\text{Fe}_{53}\text{Co}_{20}\text{Cu}_2\text{Mo}_2\text{B}_7$ sample we measured 670 kAm^{-1} .

To explain the magnetic hardening effect, EDX mappings of the quenched and the annealed $\text{Nd}_{16}\text{Fe}_{53}\text{Co}_{20}\text{Cu}_2\text{Mo}_2\text{B}_7$ samples with the highest coercivity are shown in Figure 6. In the quenched state (Figure 6, left column) the Cu is mainly found within the Nd-rich grain-boundary phase (Figure 6e, green contrast) while traces of Co (Figure 6c) and Mo (Figure 6g) can be found in the metastable $\text{Nd}_2(\text{Fe},\text{Co})_{17}\text{B}_x$ phase, and some Co is also found within the grain-boundary phase. After the heat treatment, the Cu remains in the Nd-rich grain-boundary phase (Figure 6f). Co was found in the $\text{Nd}_2(\text{Fe},\text{Co})_{14}\text{B}$ grains and the secondary intermetallic phases (Figure 6d). The key difference was the Mo distribution (Figure 6h). Mo does not enter the hard-magnetic $\text{Nd}_2(\text{Fe},\text{Co})_{14}\text{B}$ phase, but locates in micrometer-sized precipitates.

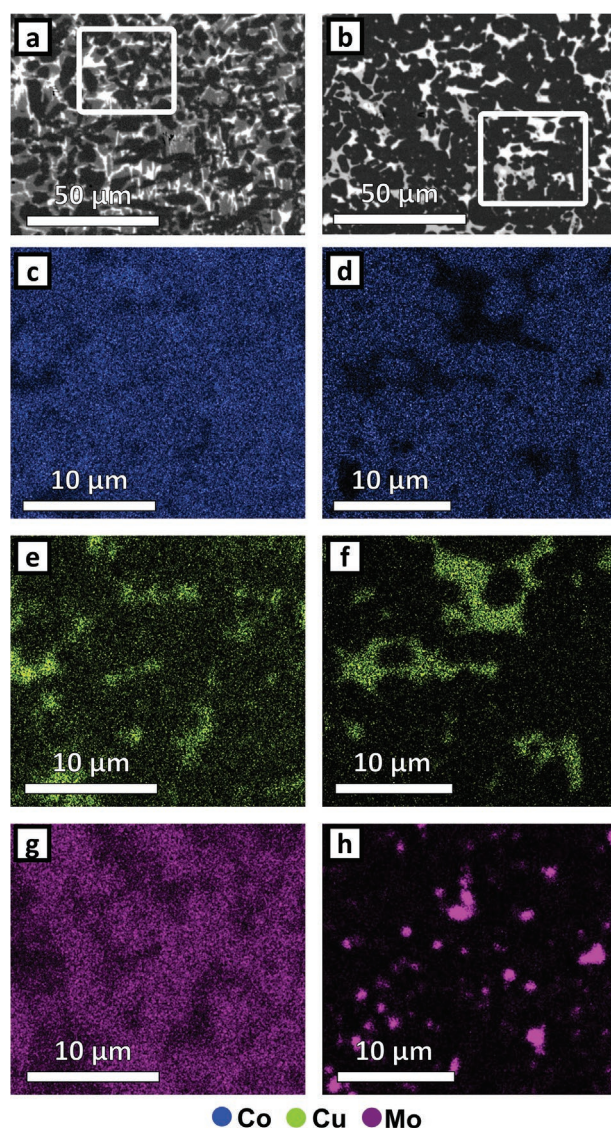


Figure 6. SEM-BSE images (a and b) and qualitative element mapping (EDX analysis – from c to h), performed on the white inset shown in a and b, of the substituting elements in quenched (left column) and annealed (right column) $\text{Nd}_{16}\text{Fe}_{53}\text{Co}_{20}\text{Mo}_2\text{Cu}_2\text{B}_7$ samples. The quenched state shows the occurrence of Co and Mo within the intermetallic grains, while Cu is localized at the grain boundary. After annealing, Co is found in the grains of hard magnetic $\text{Nd}_2(\text{Fe},\text{Co})_{14}\text{B}$ phase. Cu is still localized within the grain boundaries, whereas Mo is segregated and localized in the precipitates.

Detailed microstructural investigation by high-resolution SEM reveals microstructural features of the $\text{Nd}_{16}\text{Fe}_{53}\text{Co}_{20}\text{Mo}_2\text{Cu}_2\text{B}_7$ sample in the quenched low-coercive state (Figure 7a,c) and after annealing in the high coercive state (Figure 7b,d).

Both samples show (Nd,Cu)-rich grain boundary regions in bright contrast, however the quenched state shows the formation of the metastable $\text{Nd}_2(\text{Fe},\text{Co})_{17}\text{B}_x$ phase which is surrounded by intermetallic $\text{Nd}(\text{Fe},\text{Co})_4\text{B}$ phase (Figure 7c). High-resolution TEM (HR-TEM) and diffraction patterns acquisitions were performed to detect the crystal structure of metastable phase (Figure 8). The diffractogram on a larger grain of

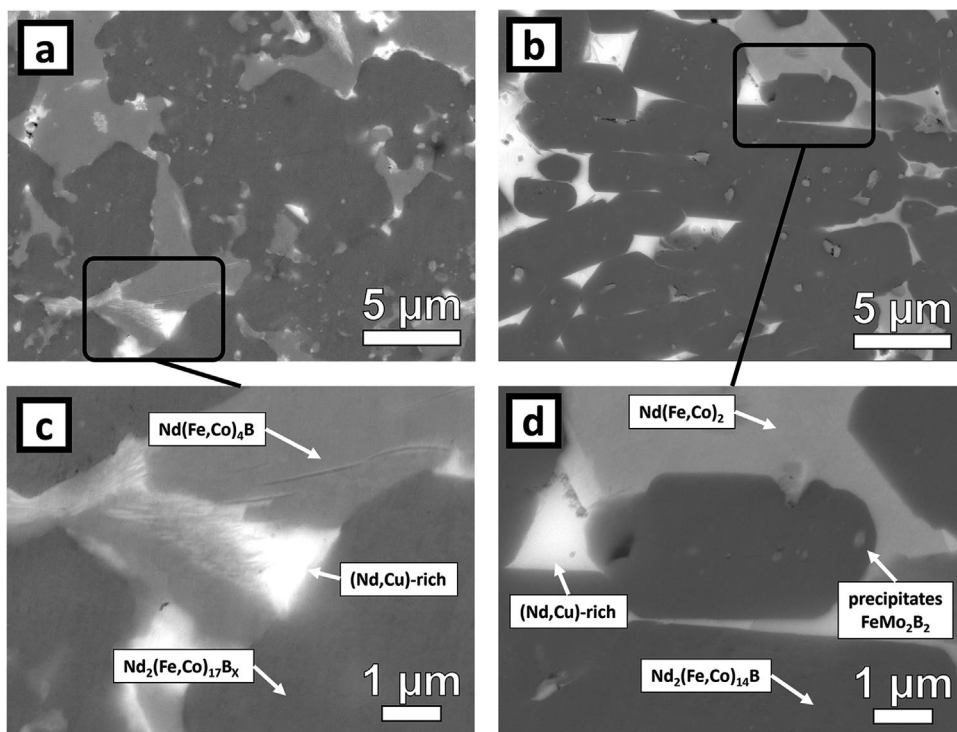


Figure 7. High resolution SEM-BSE images of the quenched $\text{Nd}_{16}\text{Fe}_{53}\text{Co}_{20}\text{Mo}_2\text{Cu}_2\text{B}_7$ sample on the left (a and c) in comparison to the annealed state (b and d). Besides the formation of the metastable $\text{Nd}_2(\text{Fe,Co})_{17}\text{B}_x$ phase, the quenched sample shows the formation of intermetallic $\text{Nd}(\text{Fe,Co})_4\text{B}$ phase and precipitates.

the metastable phase can be assigned to [1-12] zone axis of the $\text{Nd}_2\text{Fe}_{17}$ structure (No. 166; R-3m), which is consistent with the XRD data.

After the annealing treatment, the hard magnetic $\text{Nd}_2(\text{Fe,Co})_{14}\text{B}$ phase and intermetallic $\text{Nd}(\text{Fe,Co})_2$ phase are observed (Figure 7d). In addition, precipitates within the hard magnetic $\text{Nd}_2(\text{Fe,Co})_{14}\text{B}$ phase are observed, which explains the local enrichments in Mo after the annealing treatment, presented in the EDX analysis in Figure 6. A more detailed microstructural characterization of the precipitates was made by using TEM (see Figure 9). Besides the micrometer-sized Morich precipitates, nano-scale precipitation within the hard-magnetic $\text{Nd}_2(\text{Fe,Co})_{14}\text{B}$ grains and the grain boundary were found in the annealed $\text{Nd}_{16}\text{Fe}_{53}\text{Co}_{20}\text{Mo}_2\text{Cu}_2\text{B}_7$ sample (Figure 9a). The sizes of the precipitates range from approximately 100 nm

(as depicted by TEM) to 3 μm (which are shown by the SEM-EDX mapping in Figure 6). Fast Fourier transform from the TEM image in (b) match the simulated diffraction pattern of FeMo_2B_2 phase with a tetragonal crystal structure (reference number 5431 in ICSD database) (No. 127; P4/mbm). Since the precipitates are known to be non-ferromagnetic, a pinning-type coercivity mechanism like that observed with $\text{Sm}_2\text{Co}_{17}$ magnets is not to be expected. This is in agreement with the initial magnetization curves measured for the thermally demagnetized samples (Figure 5).

The magnetic domain structure of the metastable $\text{Nd}_2(\text{Fe,Co})_{17}\text{B}_x$ phase and the stable $\text{Nd}_2(\text{Fe,Co})_{14}\text{B}$ phase can be visualized using magneto-optical Kerr microscopy. The domain patterns were observed on arbitrarily oriented polished surfaces of isotropic samples. In the as-quenched sample there is

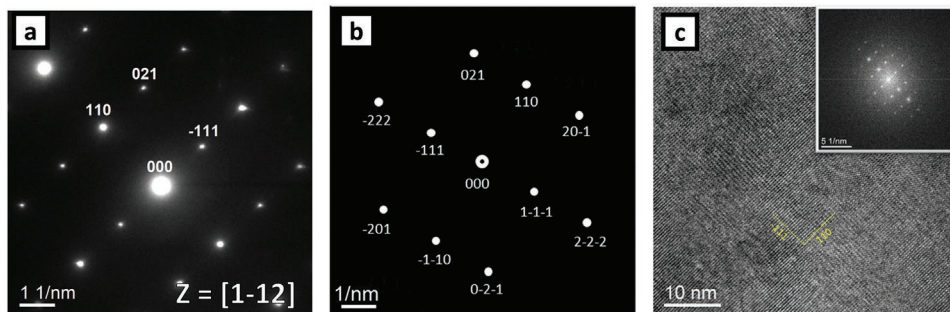


Figure 8. TEM investigation on a metastable $\text{Nd}_2(\text{Fe,Co})_{17}\text{B}_x$ grain with a) diffraction pattern and indexed intensities along the $Z = [1-12]$ zone axis together with the b) simulated diffraction pattern of the $\text{Nd}_2\text{Fe}_{17}$ structure according to the XRD measurement and c) the corresponding HR-TEM image with an insert of the FFT intensities.

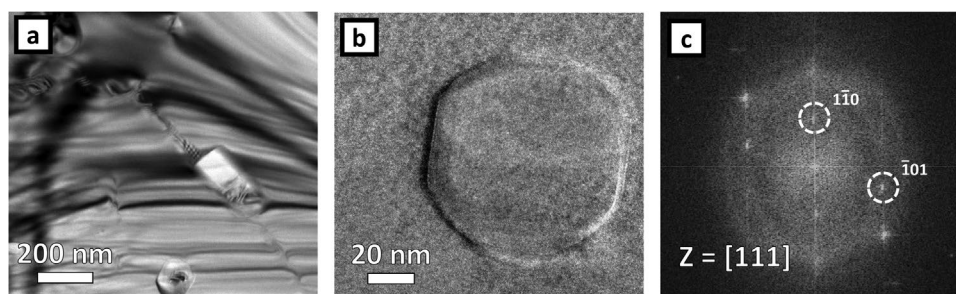


Figure 9. TEM images of the FeMo_2B_2 precipitates in the annealed $\text{Nd}_{16}\text{Fe}_{53}\text{Co}_{20}\text{Mo}_2\text{Cu}_2\text{B}_7$ sample. Image a) shows a triple junction between neighboring $\text{Nd}_2(\text{Fe},\text{Co})_{14}\text{B}$ grains with precipitates in the grain boundary and the grain interior. Image b) shows a precipitate and a non-epitaxial interface to the $\text{Nd}_2(\text{Fe},\text{Co})_{14}\text{B}$ matrix phase. Image c) shows the diffraction pattern of the precipitate in image b) along the zone axis $Z = [111]$ and the indexed crystallographic planes of the tetragonal FeMo_2B_2 structure.

a lack of uniaxial magnetocrystalline anisotropy, which leads to poorly defined domain patterns in the grains of the metastable $\text{Nd}_2(\text{Fe},\text{Co})_{17}\text{B}_x$ phase (Figure 10a). The contrast with the $\text{Nd}_2(\text{Fe},\text{Co})_{14}\text{B}$ phase (Figure 10b) is very obvious, where depending on the crystallographic orientations of the grains, stripe or a branch-type magnetic domains can be seen inside the $\text{Nd}_2(\text{Fe},\text{Co})_{14}\text{B}$ phase after annealing.

The increase in coercivity with the addition of Mo in Nd-Fe-B based alloys was reported by Shen et al.^[40] They described an increased nucleation field necessary for reverse magnetic domains around the Mo-rich precipitates as the reason for the increase in coercivity with increasing Mo content in sintered Nd-Fe-Co-B alloys. Our investigation cannot prove this assumption since many changes in the microstructure (grain size and phases) were observed that could lead to the enhancement in coercivity. Moreover, the grain-refining effect during the transformation of the $\text{Nd}_2(\text{Fe},\text{Co})_{17}\text{B}_x$ to the hard-magnetic $\text{Nd}_2(\text{Fe},\text{Co})_{14}\text{B}$ grains would appear to be an obvious reason for increased coercivity. The precipitates could be acting as nucleation sites for the $\text{Nd}_2(\text{Fe},\text{Co})_{14}\text{B}$ phase during the transformation from the metastable phase. Because of their paramagnetic properties, an influence on the magnetic properties is not to be expected. In contrast to the effective annealing treatment during the thermomagnetic measurements, where the α -(Fe,Co) phase was detected on the cooling curves (Figure 4), the controlled temperature profile during the annealing of the bulk alloys

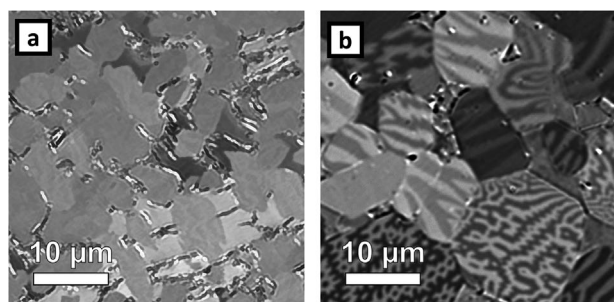


Figure 10. Kerr microscopy of the a) quenched and b) the annealed $\text{Nd}_{16}\text{Fe}_{53}\text{Co}_{20}\text{Mo}_2\text{Cu}_2\text{B}_7$ samples. In the quenched sample, the weak Kerr contrast in the metastable $\text{Nd}_2(\text{Fe},\text{Co})_{17}\text{B}_x$ phase indicates the non-uniaxial magnetocrystalline anisotropy of this phase. In contrast, annealing leads to the formation of the hard magnetic $\text{Nd}_2(\text{Fe},\text{Co})_{14}\text{B}$ phase with strong uniaxial magnetocrystalline anisotropy and pronounced Kerr contrast.

does not lead to the formation of the α -(Fe,Co) phase, rather it crystallizes the hard magnetic $\text{Nd}_2(\text{Fe},\text{Co})_{14}\text{B}$, making it a crucial step in the magnetic hardening.

4. Conclusion

Our experiments highlight the formation of a metastable $\text{Nd}_2(\text{Fe},\text{Co})_{17}\text{B}_x$ phase in the Nd-Fe-B system during the quenching of small samples into water. The samples containing this metastable phase have a low coercivity of $\approx 200 \text{ kAm}^{-1}$. After subsequent annealing at $1075 \text{ }^\circ\text{C}$ for 30 min and $500 \text{ }^\circ\text{C}$ for 60 min, the transformation of the metastable $\text{Nd}_2(\text{Fe},\text{Co})_{17}\text{B}_x$ phase into the hard magnetic $\text{Nd}_2(\text{Fe},\text{Co})_{14}\text{B}$ phase leads to a new microstructure and an increase in the coercivity to $\approx 670 \text{ kAm}^{-1}$ – more than three times higher.

Figure 11 shows the grain sizes of the samples after annealing and the fraction of metastable $\text{Nd}_2(\text{Fe},\text{Co})_{17}\text{B}_x$ phase in the as-cast samples for all the investigated alloys and the corresponding coercivity obtained after subsequent annealing and the transformation of the metastable $\text{Nd}_2(\text{Fe},\text{Co})_{17}\text{B}_x$ phase into the $\text{Nd}_2(\text{Fe},\text{Co})_{14}\text{B}$ phase. The addition of Mo and Cu leads to a grain refinement after annealing. However, the coercivity increase is not only driven by this reduced grain size. The elements Co, Mo, and Cu are necessary to stabilize the $\text{Nd}_2(\text{Fe},\text{Co})_{17}\text{B}_x$ phase, which is the starting point for the subsequent solid-state transformation. Therefore, the combination of all three elements (Co, Mo, and Cu) is required to increase the fraction of $\text{Nd}_2(\text{Fe},\text{Co})_{17}\text{B}_x$ phase in as-cast samples and so increase in the coercivity after subsequent annealing. In addition, in the annealed $\text{Nd}_{16}\text{Fe}_{53}\text{Co}_{20}\text{Mo}_2\text{Cu}_2\text{B}_7$ sample we detected the formation of FeMo_2B_2 precipitates, which we believe to be responsible for the grain-refining effect and the high coercivity of this sample.

Our findings point to a new route to obtaining high-coercivity Nd-Fe-B magnets that does not require comminution (the sintered route) or externally applied mechanical forces (the hot-pressed route). The metastable phase formation and subsequent solid-state phase transformation open up great opportunities for obtaining a high coercive state in Nd-Fe-B-based alloys. We have demonstrated the effect using a Nd-Fe-Co-Mo-Cu-B alloy, however exploiting this mechanism can unveil new routes in magnet production and improve the properties of additively manufactured magnets, as well as commercially produced Nd-Fe-B magnets.

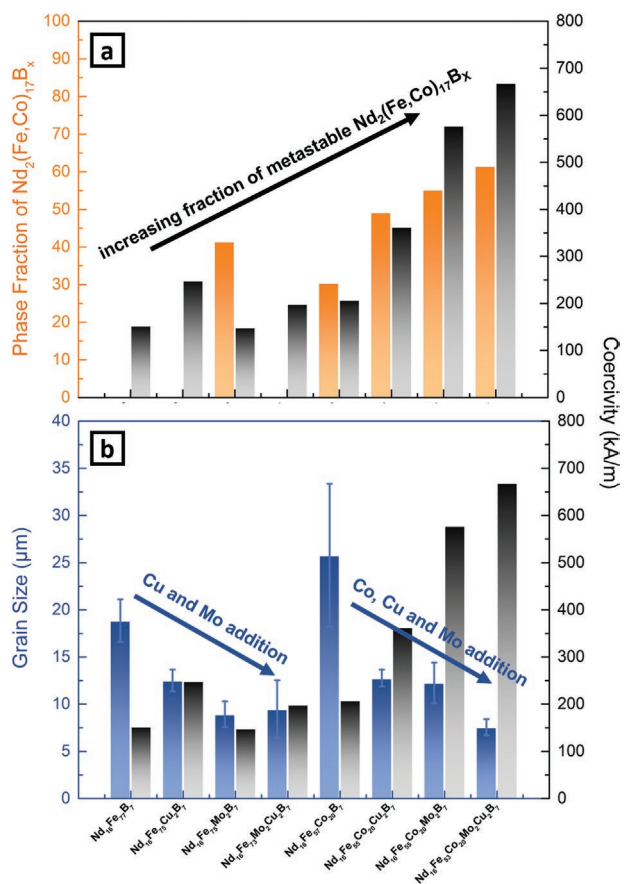


Figure 11. a) Fraction of metastable $\text{Nd}_2(\text{Fe,Co})_{17}\text{B}_x$ phase in as-cast samples for all investigated alloys (left axis) and the corresponding coercivity obtained in these alloys after subsequent annealing (right axis). Annealing leads to the transformation of the metastable $\text{Nd}_2(\text{Fe,Co})_{17}\text{B}_x$ phase into the $\text{Nd}_2(\text{Fe,Co})_{14}\text{B}_x$ phase and magnetic hardening of the samples. b) Grain size in comparison to the coercivity after the annealing treatment. For the two series of samples, Cu and Mo show grain-refining effects. Only the addition of all three elements (Co, Cu, and Mo) leads to smallest grain size and highest coercivity.

5. Experimental Section

The eight alloys $\text{Nd}_{16}\text{Fe}_{\text{bal-x-y-z}}\text{Co}_x\text{Mo}_y\text{Cu}_z\text{B}_7$ (with $x = 0; 20; y = 0; 2$ and $z = 0; 2$) were prepared by induction melting stoichiometric amounts of high-purity elements under an argon atmosphere. For the annealing, the ingots were crushed into smaller pieces with random geometry (2–4 mm in diameter) and sealed in quartz ampules with an argon atmosphere.

First, the quartz ampules were introduced to a furnace at 1300 °C. The samples were remelted for 10 min and subsequently quenched by dropping the ampules into room-temperature water for the fastest cooling rate. These quenched pieces were cut into two halves. One half was used for the metallographic characterization and for thermomagnetic measurements of the as-quenched samples. The second half of the quenched samples was sealed again in quartz ampules under argon and heat treated. The annealing process included a high-temperature annealing at 1075 °C for 30 min, followed by cooling with 300 K h⁻¹ to 500 °C, dwell for one hour and furnace cooling to room temperature.

For the determination of the microstructural features and phase analysis, the samples were embedded in a conductive polymer resin, followed by metallographic preparation. The microstructure and phase analyses were conducted with a scanning electron microscope (Tescan VEGA 3 SEM and JEOL JSM-7600F) with a tungsten cathode. Backscattered electrons (BSE) were used to highlight the different phases. In addition,

energy-dispersive X-ray spectroscopy (EDX) was employed to quantify the local composition and to visualize the elemental distribution. The quantitative phase fractions were determined using ImageJ and a Trainable Weka Segmentation script^[39] on the SEM-BSE images. The grain size was manually quantified with the line-intersection method using the SEM-BSE images. The uncertainties are given in the corresponding graphs.

For the crystallographic analysis, the samples were characterized by X-ray powder diffraction (XRD). The measurements were carried out on a Stoe Stadi P diffractometer with Mo $K_{\alpha 1}$ radiation, in transmission mode and an angular 2θ range from 5° to 50°. Phase matching and quantification via Rietveld analysis were performed using the FullProf software package.^[41]

Nanoscale characterizations of the metastable phase were done using a 200 kV JEOL JEM 2100-F Transmission Electron Microscope (TEM). The TEM lamella was prepared by cutting a slice of approximately 10 mm thickness of a bulk sample. The slice was then polished down to 50 µm thickness. Subsequent thinning down to an electron transparent lamella was achieved by ion milling a two-step process using a Gatan 691 Precision Ion Polishing System (PIPS). First, the angles and ion beam energy were set to 8 and 5.5 eV, respectively, and milling was done until a small hole was observed in the sample center. Then, the second step of milling with angles of 2° and ion beam energy of 2 eV was done to remove the damages from the previous step of milling. The structural features were investigated using bright-field and high-resolution TEM imaging, and diffraction patterns.

For the annealed samples, TEM was performed on an aberration-corrected Titan 80–300 microscope (FEI Company). The specimens for the TEM study were prepared on an FEI Strata 400S dual-beam facility. The indexing of the FFT patterns was done using the JEMS software (P. Stadelmann).

The magnetic hysteresis loops of the samples were measured inside a Quantum Design Physical Properties Measurement System PPMS-14 with the VSM option at room temperature in a maximum field of 3 T. Thermomagnetic measurements were carried out using a LakeShore 7410 Vibrating Sample Magnetometer (VSM) equipped with an oven option. The magnetization was measured during heating and cooling between 350 to 1200 K with a heating rate of 5 K min⁻¹ and a constant applied field of 0.05 T. Before and after the thermomagnetic measurements, a magnetic hysteresis was recorded in a field of 2 T at room temperature to check the quality of the sample before and after the thermomagnetic measurements. Degradation of the sample due to oxidation would lead to a decrease, whereas the formation of Fe phase leads to an increase in the saturation magnetization.

Supporting Information

Supporting Information is available from the Wiley Online Library or from the author.

Acknowledgements

The authors would like to thank the Collaborative Research Centre/Transregio 270 HoMMage and all project partners for the fruitful discussions and scientific input. This work was supported by the Deutsche Forschungsgemeinschaft (DFG, German Research Foundation), Project ID No. 405553726, TRR 270, projects A01, A10, B04, and Z01. Furthermore, this work was partly performed with the support of the Karlsruhe Nano Micro Facility (KNMF), a Helmholtz Research Infrastructure at the Karlsruhe Institute of Technology (KIT). The unit was corrected in Section 2, page 2 and Section 5, page 9, from 300 K min⁻¹ to 300 K h⁻¹, on January 20th, 2023, after the initial online publication.

Open access funding enabled and organized by Projekt DEAL.

Conflict of Interest

The authors declare no conflict of interest.

Data Availability Statement

The data that support the findings of this study are available from the corresponding author upon reasonable request.

Keywords

coercivity, magnetic hardening, metastable phases, Nd-Fe-B, rapid solidification, solid-state phase transformations

Received: August 1, 2022

Revised: October 21, 2022

Published online: November 27, 2022

-
- [1] S. Sugimoto, *J. Phys. D: Appl. Phys.* **2011**, *44*, 064001.
- [2] S. Hirose, *IEEE Trans. Magn.* **2019**, *55*, 1.
- [3] O. Gutfleisch, M. A. Willard, E. Brück, C. H. Chen, S. G. Sankar, J. P. Liu, *Adv. Mater.* **2011**, *23*, 821.
- [4] K. Opelt, T. Ahmad, O. Diehl, M. Schönfeldt, E. Brouwer, I. Vogel, J. D. Rossa, J. Gassmann, S. Ener, O. Gutfleisch, *Adv. Eng. Mater.* **2021**, 2100459.
- [5] K. Hono, H. Sepehri-Amin, *Scr. Mater.* **2012**, *67*, 530.
- [6] L. Q. Yu, R. S. Liu, K. T. Dong, Y. P. Zhang, *Transw. Res. Netw.* **2012**, *667*, 1.
- [7] J. Wecker, L. Schultz, *Appl. Phys. Lett.* **1987**, *51*, 697.
- [8] K. Hioki, *Sci. Technol. Adv. Mater.* **2021**, *22*, 72.
- [9] H. Kronmüller, K.-D. Durst, M. Sagawa, *J. Magn. Magn. Mater.* **1988**, *74*, 291.
- [10] J. Fidler, T. Schrefl, *J. Appl. Phys.* **1996**, *79*, 5029.
- [11] F. Bittner, J. Thielsch, W.-G. Drossel, *Prog. Addit. Manuf.* **2020**, *5*, 3.
- [12] D. Goll, F. Trauter, T. Bernthaler, J. Schanz, H. Riegel, G. Schneider, *Micromachines* **2021**, *12*, 538.
- [13] L. Schäfer, K. Skokov, J. Liu, F. Maccari, T. Braun, S. Riegg, I. Radulov, J. Gassmann, H. Merschroth, J. Harbig, M. Weigold, O. Gutfleisch, *Adv. Funct. Mater.* **2021**, *31*, 2102148.
- [14] D. Goll, F. Trauter, P. Braun, J. Laukart, R. Loeffler, U. Golla-Schindler, G. Schneider, *Phys. Status Solidi R. R. L.* **2021**, *15*, 2100294.
- [15] P. F. Rottmann, A. T. Polonsky, T. Francis, M. G. Emigh, M. Krispin, G. Rieger, M. P. Echlin, C. G. Levi, T. M. Pollock, *Mater. Today* **2021**, *49*, 23.
- [16] J. Gao, T. Volkmann, D. M. Herlach, *IEEE Trans. Magn.* **2002**, *38*, 2910.
- [17] J. Strohmenger, T. Volkmann, J. Gao, D. M. Herlach, *Mater. Sci. Forum* **2006**, *508*, 81.
- [18] T. Volkmann, J. Gao, J. Strohmenger, D. M. Herlach, *Mater. Sci. Eng. A* **2004**, *375–377*, 1153.
- [19] J. Gao, T. Volkmann, D. M. Herlach, *J. Alloys Compd.* **2003**, *350*, 344.
- [20] J. Gao, T. Volkmann, D. M. Herlach, *Acta Mater.* **2002**, *50*, 3003.
- [21] J. Gao, T. Volkmann, J. Strohmenger, D. M. Herlach, *Mater. Sci. Eng. A* **2004**, *375–377*, 498.
- [22] S. Ozawa, K. Kuribayashi, S. Hirose, S. Reutzel, D. M. Herlach, *J. Appl. Phys.* **2006**, *100*, 123906.
- [23] J. Gao, B. Wei, *J. Alloys Compd.* **1999**, *285*, 229.
- [24] R. Hermann, W. Löser, *J. Appl. Phys.* **1998**, *83*, 6399.
- [25] J. Gao, T. Volkmann, S. Roth, W. Löser, D. M. Herlach, *J. Magn. Magn. Mater.* **2001**, *234*, 313.
- [26] S. Ozawa, M. Li, S. Sugiyama, I. Jimbo, S. Hirose, K. Kuribayashi, *Mater. Sci. Eng. A* **2004**, *382*, 295.
- [27] J. Gao, T. Volkmann, D. M. Herlach, *J. Alloys Compd.* **2000**, *308*, 296.
- [28] S. Ozawa, M. Li, S. Sugiyama, I. Jimbo, K. Kuribayashi, *Mater. Trans.* **2003**, *44*, 806.
- [29] S. Ozawa, T. Saito, T. Motegi, *J. Alloys Compd.* **2004**, *363*, 268.
- [30] K. Kuribayashi, S. Ozawa, *J. Alloys Compd.* **2006**, *408–412*, 266.
- [31] Y. K. Zhang, J. Gao, H. Yasuda, D. M. Herlach, J. C. He, *J. Alloys Compd.* **2010**, *493*, L8.
- [32] J. Gao, T. Volkmann, D. M. Herlach, *J. Mater. Res.* **2001**, *16*, 2562.
- [33] J. Strohmenger, T. Volkmann, J. Gao, D. M. Herlach, *Mater. Sci. Eng. A* **2005**, *413–414*, 263.
- [34] A. Z. Sun, S. Wu, W. H. Xu, J. Wang, Q. Zhang, F. Q. Zhai, A. A. Volinsky, *Int. J. Miner., Metall. Mater.* **2012**, *19*, 236.
- [35] C. D. Fuerst, J. F. Herbst, *J. Appl. Phys.* **1988**, *63*, 3324.
- [36] J. Wecker, L. Schultz, *Appl. Phys. Lett.* **1987**, *51*, 697.
- [37] C. B. Rong, D. Wang, V. Van Nguyen, M. Daniil, M. A. Willard, Y. Zhang, M. J. Kramer, J. P. Liu, *J. Phys. D: Appl. Phys.* **2013**, *46*, 045001.
- [38] C. D. Fuerst, J. F. Herbst, *J. Appl. Phys.* **1988**, *63*, 3324.
- [39] I. Arganda-Carreras, V. Kaynig, C. Rueden, K. W. Eliceiri, J. Schindelin, A. Cardona, H. S. Seung, *Bioinformatics* **2017**, *33*, 2424.
- [40] X. Shen, Y. Wang, Z. Diao, X. Liu, *J. Appl. Phys.* **1987**, *61*, 3433.
- [41] J. Rodríguez-Carvajal, *Phys. B: Condens. Matter* **1993**, *192*, 55.